

Sepehr Nesaei

School of Mechanical and Materials Engineering,
Washington State University,
405 NE Spokane Street,
Pullman, WA 99164
e-mail: sepehr.nesaei@wsu.edu

Mitch Rock

School of Mechanical and Materials Engineering,
Washington State University,
405 NE Spokane Street,
Pullman, WA 99164
e-mail: darman.rock@wsu.edu

Yu Wang

School of Mechanical and Materials Engineering,
Washington State University,
405 NE Spokane Street,
Pullman, WA 99164
e-mail: yu.wang3@wsu.edu

Michael R. Kessler

School of Mechanical and Materials Engineering,
Washington State University,
405 NE Spokane Street,
Pullman, WA 99164
e-mail: michaelr.kessler@wsu.edu

Arda Gozen¹

School of Mechanical and Materials Engineering,
Washington State University,
405 NE Spokane Street,
Pullman, WA 99164
e-mail: arda.gozen@wsu.edu

Additive Manufacturing With Conductive, Viscoelastic Polymer Composites: Direct-Ink-Writing of Electrolytic and Anodic Poly(Ethylene Oxide) Composites

Conductive viscoelastic polymer composites (CVPCs) consisting of conductive fillers in viscoelastic polymer matrices find numerous applications in emerging technologies such as flexible electronics, energy storage, and biochemical sensing. Additive manufacturing methods at micro- and mesoscales provide exciting opportunities toward realizing the unique capabilities of such material systems. In this paper, we study the direct-ink-writing (DIW) process of CVPCs consisting of electrically conductive additives in a poly(ethylene oxide) (PEO) matrix. We particularly focus on the deposition mechanisms of the DIW process and the influence of these mechanisms on the printed structure geometry, morphology, and functional properties. To this end, we utilized a novel practical approach of modeling the ink extrusion through the nozzles considering the non-Newtonian viscous effects while capturing the viscoelastic extensional flow (drawing) effects through the variation of the nozzle exit pressure. We concluded that inks containing higher amounts of high molecular weight (HMW) PEO exhibit drawing type deposition at high printing speeds and low inlet pressures enabling thinner, higher aspect ratio structures with ideal three-dimensional stacking. Under this deposition mechanism, the electrical conductivity of the anodic structures decreased with increasing printing speed, indicating the effect of the drawing mechanism on the printed structure morphology. [DOI: 10.1115/1.4037238]

Introduction

Polymer nanocomposites are an emerging class of material systems that incorporate micro-to-nanoscale fillers in polymer matrices. These material systems combine the favorable properties of the fillers and the matrix to obtain multifunctional parts and devices that cannot be realized through single phase materials. One of the most common examples of this implementation is polymer composites that incorporate conductive species such as carbon black [1], carbon nanotubes [2–4], graphene [5], and graphene oxide [6], metal nanoparticles [7], or ionically conductive compounds [8] in highly viscoelastic matrices. These material systems are referred to as conductive viscoelastic polymer composites (CVPC). The type, chemistry, and the concentration of the fillers in CVPCs can be tuned to realize wide range of electrical and thermal conductivities combined with high mechanical compliance. Such systems are utilized in a wide range of application areas including flexible electronics [1,4,6], energy storage and conversion [8–12], biochemical sensing [2], etc. Techniques used to process viscoelastic conductive polymer composites play a critical role in the performance of the functional components fabricated from such materials by directly determining their geometry and morphology [13]. As such, realizing the full potential of these unique material systems requires a comprehensive research effort in the relevant fabrication methods.

Recent emergence of the additive manufacturing methods provided unique opportunities for a wide range of material systems including CVPCs. Among these methods, the most relevant to CVPCs are the direct-write methods involving controlled deposition of materials along precisely controlled paths and complex three-dimensional architectures at size scales ranging from millimeter to submicron scales [14]. The typical properties of CVPCs such as high viscosity at low-shear rates ($\sim 10^3$ to 10^5 Pa·s) with shear thinning and viscoelastic behavior with high extensional relaxation times (>1 s) prevents their processing using discrete direct-write methods such as ink-jet or aerosol jet printing [15]. However, direct-write methods involving continuous flow and deposition of inks derived from materials of interest, such as direct-ink-writing (DIW) [16,17], fiber drawing [4,18–21], and electrohydrodynamic printing [22–25], have been widely used to process CVPCs. These approaches enable the highest feature resolution and geometric complexity which are critical for many applications including sensing and energy storage [10,11]. Furthermore, they provide the unique capability of creating functionally graded structures with precisely controlled property gradients. Understanding of how the fabricated structure properties are affected by CVPC ink properties and the deposition mechanisms is essential for effective utilization of these unique capabilities. To date, there are only a few studies focusing on this fundamental understanding [6,26].

Two main types of deposition mechanisms are observed during continuous direct writing of inks with rheological behavior similar to that of the CVPCs as illustrated in Fig. 1(a). Both cases involve the flow of the inks through micro-to-mesoscale nozzles but are differentiated through the excitation of this flow. In the extrusion

¹Corresponding author.

Manuscript received March 13, 2017; final manuscript received June 18, 2017; published online September 13, 2017. Assoc. Editor: Zhijian J. Pei.

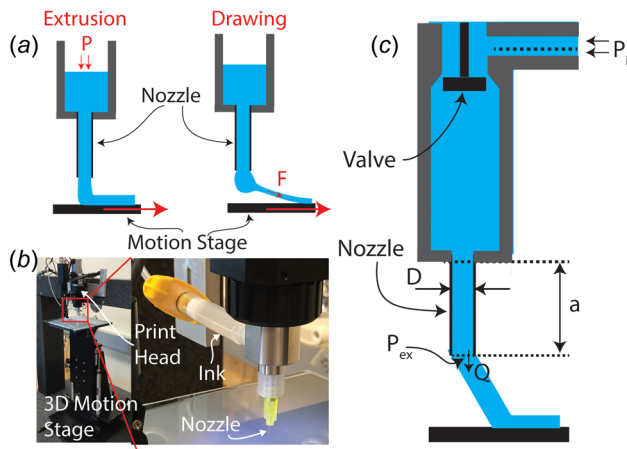


Fig. 1 DIW process and system details: (a) two different regimes of DIW, (b) the DIW system used in this study, and (c) schematic description of the ink flow path during the DIW

case, which is the main deposition mechanism of DIW, the inks are “pushed out” of the nozzles by positive pressure. Non-Newtonian flow under high shear rate primarily drives the extrusion mechanism. In drawing, the ink is “pulled out” of the nozzle under the effect of external forces, as primarily observed in fiber drawing, polymer spinning, or electrohydrodynamic printing. The drawing mechanism is primarily driven by the ink viscoelasticity and extensional flow. The fabrication methods involving the drawing mechanism have been shown to enable filaments of submicron diameters to be generated due to the extensional flow and the associated radial compression of the dispensed material [27,28]. Extrusion-based DIW usually exhibits lower resolution (tens to hundreds of microns of filament diameters) but provides higher spatial accuracy and repeatability. All the continuous direct-write methods share a common hardware configuration consisting of a pressurized ink reservoir, a nozzle, and motion system as depicted in Fig 1(b). As such, the mode of flow and deposition is determined by material properties and a set of process parameters including reservoir pressure, printing speed, nozzle–substrate distance, and substrate’s electrical potential [25]. The fundamental models of these individual methods, within their specific parameter space and for relevant materials, have been devised in the literature. In the case of DIW, these efforts primarily aim to correlate the relevant ink properties to their flow rate and final printed geometry under various processing conditions. The DIW models focus on the shear rheology of the inks and its impact on their non-Newtonian flow during the process [29–31] or viscoelastic properties such as elastic and loss moduli and their variation with certain processing parameters such as temperature [32]. Only a limited number of studies looked into the geometry of the deposited material flowing its extrusion [30,33]. For fiber drawing, most studies focused on the prediction of the fiber diameter and its empirical correlation to the extensional rheology and capillary properties of the ink [21].

Despite the established understanding of these individual flow and deposition mechanisms, there is a lack of studies focusing on fundamentals of the transition between them or the intermediate process parameter ranges where the different modes of deposition could be observed simultaneously. A complete understanding of this critical regime of continuous direct-writing is needed for controlled transition between different modes which can broaden the capabilities of such processes and enable unique designs such as hierarchical structures with various size scales. Furthermore, for composite inks such as CVPCs, understanding the effect of different process regimes on the morphology of such species is critical in understanding the final printed material properties.

To address this research need, in this paper we present a case study of the DIW process of CVPCs consisting of conductive

species in a poly(ethylene oxide) (PEO) matrix. PEO-based CVPCs have been widely used in solid-state batteries as electrolyte and electrode materials [8,9,34,35] or interconnects in flexible electronic architectures [4]. Here, we study two types of inks: electrolytic ones that only contain LiClO₄ as the conductive species and the anodic ones that also contain graphite particles. Polymer matrix for these inks consisted of blend of two types of PEO with different molecular weights. We varied the amount of high molecular weight PEO to tune the viscoelasticity of the inks and induce different deposition mechanisms during DIW. Inspired by the recent studies in the literature where high molecular weight (HMW) PEO is used to realize conductive nanofiber drawing [4], we hypothesize here that increasing amount of HMW PEO will lead to increased drawing effects during DIW. To quantitatively determine the contribution of extrusion and drawing mechanisms, we utilized a novel method where the ink flow is modeled as non-Newtonian viscous flow, and the viscoelastic effects and thus the presence of the drawing mechanism are monitored through the variation of the nozzle exit pressure. Through this approach, we studied the effect of deposition mechanism variation in minimum input pressure for continuous deposition, geometry, morphology, and electrical conductivity of the printed structures. In the rest of this paper, we first present the experimental details of the study, followed by the results and discussions regarding the rheology and DIW of electrolytic and anodic materials, respectively.

Experimental Section

Inks and Their Preparation. The ink formulations used in this study were inspired by the authors’ earlier works on hybrid solid–liquid Li-ion battery components [8,9,35]. Electrolytic inks consisted of PEO of varying molecular weights and lithium salt (LiClO₄) dissolved in acetonitrile. A combination of two types of PEO powders was used: the low molecular weight (LMW) PEO with average molecular weight of 1×10^5 g/mol and a high molecular weight (HMW) PEO with an average molecular weight of 5×10^6 g/mol. PEO and the lithium salt were acquired from Sigma Aldrich (St. Louis, MO). The weight ratio of the lithium salt to total PEO was selected to be 1:3.3 which is the crystallization limit of the lithium salt as identified in the literature [8]. Total solute concentration in electrolytic inks was 26% w/w. Anodic inks included graphite particles (MTI Corporation, Richmond, CA, 1–5 μm granularity) in addition to the electrolytic inks. The total solid concentration (PEO, lithium salt, and graphite) for anodic inks was 41.1% w/w with 20.5% w/w graphite. Table 1 summarizes the inks that were used in this study and their compositions. Here, EL and AN descriptors highlight the type of ink used. The number following the descriptor indicates the PEO molecular weight composition. For instance, EL2 corresponds to an electrolytic ink that includes a combination of HMW to LMW PEO ratio of 2:100 w/w. Higher than 3% HMW PEO addition leads to inks having viscosities too high for successful dispersion and solution of different ink components.

To prepare the inks, solutions of two PEO types along with the lithium salt (1:3.3 w/w as detailed earlier) were prepared in

Table 1 Composition of different inks used in this study. Numbers are given in weight percentage.

| | HMW PEO | LMW PEO | LiClO ₄ | Graphite | Acetonitrile |
|-----|---------|---------|--------------------|----------|--------------|
| EL0 | — | 19.95 | 6.05 | — | 74.00 |
| EL1 | 0.198 | 19.75 | 6.05 | — | 74.00 |
| EL2 | 0.391 | 19.56 | 6.05 | — | 74.00 |
| EL3 | 0.581 | 19.37 | 6.05 | — | 74.00 |
| AN0 | — | 15.86 | 4.81 | 20.76 | 58.57 |
| AN1 | 0.157 | 15.70 | 4.81 | 20.76 | 58.57 |
| AN2 | 0.311 | 15.54 | 4.81 | 20.76 | 58.57 |
| AN3 | 0.461 | 15.39 | 4.81 | 20.76 | 58.57 |

acetonitrile. The HMW PEO + lithium salt solutions had a solute concentration of 2.6% w/w, whereas the LMW PEO + lithium salt solutions had a solute concentration of 36% w/w. These solutions were prepared by mixing the components using a compact digital mixer (Cole-Parmer, Vernon Hills, IL) compact digital mixer system, 50–2500 rpm, 115 VAC) for 10–15 min at 350–450 rpm followed by magnetic stirring for 5 h. These two solutions were then mixed in appropriate ratios to achieve the mass concentrations of different components given in Table 1. To form the anodic inks, the graphite powder was dispersed in electrolytic solutions using the high-speed mixer followed by gentle magnetic stirring. The prepared inks were stored in a desiccator cabinet at 15% relative humidity to prevent water absorption by PEO, which is known to be hygroscopic.

Characterization of the Ink Rheology. Rheological properties were tested using a strain-controlled rheometer (TA Instruments, New Castle, DE, ARES-G2) equipped with a cone and plate geometry (50 mm diameter and 0.0196 rad cone angle). Two different tests were applied to all the inks: an amplitude sweep test to characterize plateau elastic and loss moduli and a flow ramp test to capture the non-Newtonian shear stress-shear rate correlation. The inks were loaded to the test setup at a volume of 0.6 ml using a syringe. Low viscosity mineral oil was applied around the circumference of the plates to avoid solvent evaporation during testing. Prior to each test, the inks were first subjected to a step stress growth test at a low-shear rate (0.1 s^{-1} for flow ramp) or a small strain (<5% for amplitude sweep) for 100 s to ensure relaxation of any stress induced from sample loading. The amplitude sweep test was conducted at a constant oscillation frequency of 50 rad/s and a strain range of 0.025–1000%. In the flow ramp test, the ink samples were subjected to a rotational shear strain with linearly increasing strain rate from 0.1 to 1000 s^{-1} over 5 min. During the flow ramp, the cone–plate distance was kept constant, and the normal forces generated during the shear rate increase were recorded. The temperature was maintained at 25 °C for all the tests.

Direct-Ink-Writing. The custom-built direct-writing system used in this study is shown in Fig 1(b). This system consists of a three-axis motion system (Aerotech, Pittsburgh, PA) ANT180-ANT130 motion stages) that is capable of positioning the substrate with submicron accuracy within a working space of 210 mm × 160 mm × 110 mm. To dispense the inks, a positive pressure pump (Nscript, Orlando, FL, smart pump) is used. Here, the inks are introduced to the pump through a pressurized 3 cc syringe barrel as shown. The pump controls the flow of the inks through a needle valve that can be positioned with 10 μm accuracy.

In this study, an input pressure and a printing speed range of 17.23–172.3 kPa (2.5–25 psi) and 30–180 mm/s are used, respectively. For each ink, minimum inlet pressure (above or equal to 17.23 kPa–2.5 psi which is the lowest achievable pressure for our printer system) for which continuous deposition is achieved at the maximum speed of 180 mm/s is determined. This pressure level is used for all the experiments for a given ink unless otherwise noted. The discontinuous printing occurs when the flow rate is so low that the ink is deposited as discrete droplets instead of a continuous line. These droplets usually have a larger diameter than the continuous lines formed at higher flow rates due to the capillary effects and localization of volume in these droplets, as shown in Figs. 8(a) and 8(b) in the Appendix. This phenomenon helps us to easily determine the discontinuous-to-continuous transition by using low-magnification optics during the process. The maximum speed of 180 mm/s is the maximum speed our printer system can achieve with reasonable accelerations. We considered the minimum speed of 30 mm/s as the lowest reasonable speed that can meet high throughput requirements of many relevant applications.

The other DIW parameters that are kept constant during the experiments include the inner nozzle diameter of 200 μm and the nozzle–substrate distance of 100 μm . The print head is also

equipped with a microscope to monitor the printing process. The substrate on which the inks were printed was prepared by spin coating a platinum-cured silicone (Smooth-on Eco-Flex 10, East Texas, PA) on a 6 in diameter glass disk.

Optical Profilometry of the Printed Structures. The geometry of the linear structures printed using the electrolytic and anodic inks was characterized using an optical profilometer (Zygo NewView 7300, Berwyn, PA) which uses white light interferometry. For each line, a 2-mm long section was measured to characterize its average height, width, and the cross-sectional area with sub-nanometers height and submicron width resolution.

Electrical Conductivity Measurements of the Printed Structures. Electrical resistance measurements of the printed anodic structures were taken to characterize their electrical conductivity. To this end, two room temperature liquid metal droplets (Eutectic Gallium Indium, nominal melting point 15 °C) were administered on center portions of the printed lines and electrical wires connected to an LCR meter (BK Precision, Yorba Linda, CA) L789D) are inserted in them (see Fig. 8 in the Appendix). The electrical resistivity that is inversely proportional to the conductivity was calculated through

$$\rho = \frac{RA}{L} \quad (1)$$

where R is the measured resistance, A is the average cross-sectional area of the lines determined through optical profilometry, and L is the distance between the measurement points.

Atomic Force Microscopy Based Quantitative Nanomechanical Characterization of the Printed Structures. An atomic force microscopy (AFM) system (Bruker, Santa Ana, CA) Dimension Icon was used to perform peak force quantitative nanomechanical characterization (PFQNM) in order to understand the mechanical and surface properties of various material phases in the printed structures. This method provides information on the mechanical deformation and adhesion of the scanned surfaces as well as conventional AFM topography [36]. Anodic structures were characterized this way through obtaining five 20 $\mu\text{m} \times 20 \mu\text{m}$ area scans from each structure of interest. To realize objective comparison of material properties, constant peak force set point and amplitude of 15.32 nN and 150 nm, respectively, were used in each scan.

Scanning Electron Microscopy (SEM) of the Printed Structures. The morphology of the printed anodic structures was observed through an environmental scanning electron microscope (FEI, Hillsboro, OR, Quanta 200 F) in low vacuum mode.

Ink Flow Model

To understand the deposition mechanisms during DIW of various inks, we incorporated ink rheological properties and the results of the printed structure profilometry to well-established non-Newtonian models for ink flow through the printing system shown in Fig. 1(c) and analyzed the pressure state at the nozzle exit. One of the critical aspects of this approach is the use of the correct rheological model describing the shear flow of the inks. Our regression analysis on the shear stress versus strain rate data obtained through flow ramp testing showed that the behavior of these inks is best represented by a power-law behavior given by

$$\tau = K\dot{\gamma}^n \quad (2)$$

where τ is the shear stress, $\dot{\gamma}$ is the shear rate, K is the consistency index, and n is the flow behavior index.

For most inks with similar rheological behavior, the following assumptions can be made: (1) the inks are incompressible, (2) the

frictional losses occurring anywhere other than the nozzle, which has a significantly lower cross-sectional area than the rest of the print-head components, are negligible, and (3) the pressure variations due to gravitational effects are negligible compared to the pressure losses inside the nozzle. Following these assumptions, the maximum shear stress the inks experience during extrusion at the nozzle wall–ink interface is given by [29]

$$\tau_{\max} = \frac{P_i - P_{\text{ex}}}{4(a/D)} \quad (3)$$

where P_i is the prescribed relative dispensing pressure (difference from atmospheric) and P_{ex} is the relative (with respect to the ambient) pressure at the exit of the nozzle. For conventional, extrusion-based DIW, P_{ex} is due to the surface tension effects and can be calculated through $2\sigma/D$, where σ is the surface tension of the ink. Here, we include an additional term (P_d) to account for any pressure drop arising from the ink fiber drawing effects (as illustrated in Fig. 1(a))

$$P_{\text{ex}} = \frac{2\sigma}{D} + P_d \quad (4)$$

The maximum shear rate the non-Newtonian ink experiences can be calculated by considering the Newtonian shear rate with the Rabinowitsch correction as

$$\dot{\gamma} = \frac{8Q(3n+1)}{\pi D^3 n} \quad (5)$$

where Q is the volumetric flow rate of the ink. To calculate the shear rate, the average volumetric flow rate Q is first calculated using the optical profilometry measurement of the printed lines as

$$Q = \frac{\int_0^L \int_0^w z(x,y) dy dx}{cL f} \quad (6)$$

where $z(x,y)$ is the height profile of the printed as a function of x and y coordinates, defined along the length and width of lines, respectively, L is the total measured length of the line, w is the measured width of the lines, f is the printing speed, and c is the volumetric solid concentration of the ink in m^3/m^3 . The concentration term is included here since the volume of the printed lines only includes the solid content of the inks after solvent evaporation. It should be noted that Eq. (6) assumes that the entire solvent evaporates from the printed lines (validated through weight measurements of the inks during solvent evaporation at room temperature) and the final solid volume has negligible porosity. The solid concentration (c) for each ink is estimated using the prescribed mass concentrations and the results of the previous studies [37] showing that the additivity principle of volume is an accurate assumption for similar polymer solutions at room temperature (see the Appendix).

Once the shear rate is calculated, the maximum shear stress the ink will experience at this shear rate can be calculated using the power-law relation given by Eq. (2). Next, Eq. (3) can be used to calculate P_{ex} for a given P_{in} and P_d can be calculated using Eq. (4). Since the surface tension of the inks presented in this study ranged from 0.0019 to 0.0131 N/m, the $2\sigma/D$ term in Eq. (4) ranges from 0.0187 to 0.0854 kPa (0.00271–0.124 psi) for a nozzle diameter of 200 μm (see Table 4 in the Appendix). These pressure levels are negligibly small compared to the P_i values used. Accordingly, it can be assumed that $P_{\text{ex}} = P_d$. For conventional filamentary extrusion where printing speed is comparable to filament exit velocity, $P_{\text{ex}} = P_d \approx 0$. For drawing-dominated deposition, $P_{\text{ex}} = P_d < 0$, since the axial tension on the filament exiting the nozzle will reduce the exit pressure to below atmospheric levels, thus inducing a “pull” effect and increasing the shear stress (as dictated by Eq. (3)) and thus the shear rate (as dictated by

Eq. (2)) and flow rate (as dictated by Eq. (5)) for a given P_{in} . It should be noted that the drawing mechanism will only occur for cases where the velocity of the ink filament exiting the nozzle is less than the printing speed. For the cases where the ink flow rate is high such that the velocity of the ink filament exiting the nozzle is less than the printing speed, one would expect $P_{\text{ex}} = P_d > 0$ due to obstruction of the flow by the substrate surface as demonstrated in earlier works [38].

Results and Discussion

Electrolytic Inks and Their Printing. The result of the rheological characterization of the electrolytic inks is shown in Fig. 2(c). The K and n values for each tested ink are given in Table 2. Here, all the inks exhibit shear thinning behavior ($n < 1$), which is more prominent for the inks containing HMW PEO. The viscosity versus shear rate plots for these inks are shown in Fig. 8(e) in the Appendix. The shear stress at a given shear rate increases consistently with increasing amount of HMW PEO.

As indicated earlier, the first step of the DIW experiments is the determination of the minimum inlet pressure (P_{in}) yielding continuous deposition. For a given inlet pressure, negligible surface tension effects, and the extrusion-only printing regime ($P_d = 0$), the maximum shear stress would be the same for all the inks tested. In this case, one would expect the flow rate to decrease from EL0 to EL3 according to Eq. (5) and the results shown in Fig. 2(c) indicate that the lower shear rates are expected from EL0–EL3 at constant shear stress. If all the other printing parameters, including the printing speed and the nozzle–substrate distance, are kept the same for different inks, it would also be expected that the minimum dispensing pressure for which continuous deposition is achieved to be less for EL0 compared to EL1, 2, and 3 under the pure extrusion mechanism. Figures 2(a) and 2(b) show the lines obtained using EL0 and EL1 under the same inlet pressure of 34.48 kPa (5 psi) indicating that observed results contradict this expectation. In fact, the minimum inlet pressure for continuous deposition for EL0 was determined to be 68.95 kPa (10 psi) for a printing speed of 180 mm/s and a nozzle–substrate distance of 100 μm , whereas EL1, 2, and 3 formed continuous lines for an inlet pressure as low as 17.23 kPa (2.5 psi) under the same conditions. This result suggests a deposition regime different than pure extrusion for the tested inks.

Figures 2(d) and 2(e) show the variation of shear rate and P_d as a function of the printing speed for each ink, respectively. As shown, a substantial exit pressure drop is observed for inks containing HMW PEO (negative P_d), pointing out the presence of the drawing effects. Furthermore, this effect seems to increase with increasing printing speed as both the shear rate and P_d decrease, both of which cannot be explained by the pure extrusion regime. This variation is not observed for EL0 at 68.95 kPa (10 psi), indicating the prevalence of the extrusion regime. This is an expected result considering the existence of higher molecular weight PEO in EL1, 2, and 3. Longer polymer chains in these inks increase the extensional viscosity and relaxation time, leading to extensional flow and elastocapillary thinning with long filament life time [39]. As such, even at low flow rates through the nozzle, EL1, 2, and 3 can maintain continuous filamentary deposition through the drawing regime. The long life span of the filaments implies that the thinning process continues for a long period of time leading to substantially finer structures than the nozzle diameter. EL0, on the other hand, exhibits substantially lower viscoelasticity and extensional viscosity, the filament stretching that occurs at low flow rates leads to viscoplastic thinning with significantly lower filament life times than elastocapillary thinning. As such, EL0 undergoes cyclic filament formation and failure during printing at low pressures, leading to discontinuous lines, as illustrated in Fig. 2(g) and demonstrated in Figs. 8(a) and 8(b) in the Appendix.

The effect of the inlet pressure on P_d was also studied at a constant printing speed of 60 mm/s for EL1, 2, and 3. As shown in

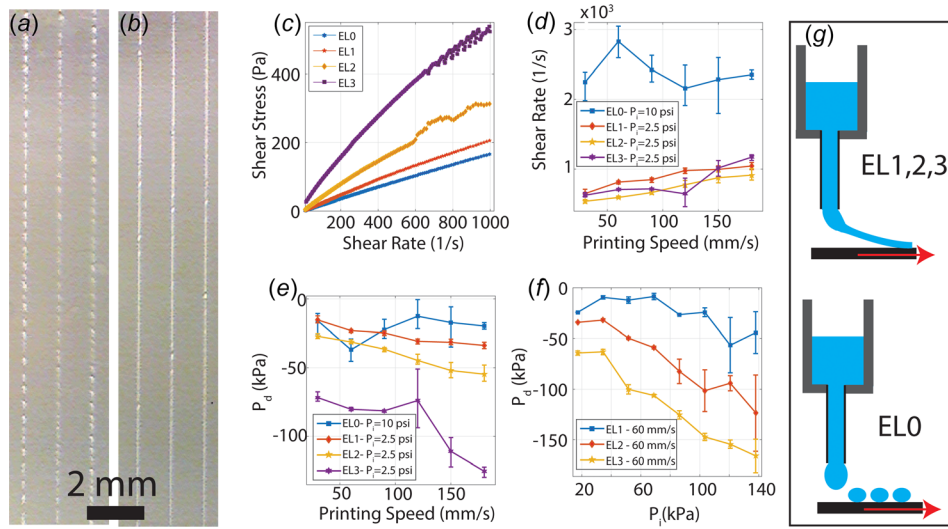


Fig. 2 Results of the DIW experiments with electrolytic inks regarding the exit pressure variation and its impact on printing: (a) lines printed using EL0 at 5 psi inlet pressure and 180 mm/s printing speed, (b) lines printed using EL3 at 5 psi inlet pressure and 180 mm/s printing speed, (c) shear rheology of the electrolytic inks, (d) shear rate of the electrolytic inks during DIW as a function of printing speed, (e) P_d values calculated for the electrolytic inks as a function of the printing speed, (f) P_d values calculated for the electrolytic inks as a function of the inlet pressure, and (g) schematic description of the two different deposition mechanisms experienced by different electrolytic inks

Table 2 Power-law coefficients for the electrolytic inks studied

| Electrolyte | K (Pa·s) | n |
|-------------|------------|-------|
| EL0 | 0.22 | 0.961 |
| EL1 | 0.324 | 0.938 |
| EL2 | 0.619 | 0.912 |
| EL3 | 3.09 | 0.749 |

Fig. 2(f), the P_d value decreased with increasing P_i in the negative range (increasing drawing effect) particularly for EL2 and 3. It would be expected that a higher inlet pressure (and the associated flow rate increase) would lead to a more extrusionlike regime, which would cause higher values of P_d as the inks start to bulge under the nozzle. The obtained results are contradictory to this postulation. One possible reason is the die-swell (Barus) effect causing volume increase of the inks containing HMW PEO as they leave the nozzle. This effect is often observed for such materials during their extrusion and becomes more prevalent as the shear rates and stresses increase due to increasing inlet pressure [39]. This volume increase leads to calculation of higher flow rates in Eq. (6), higher shear rate in Eq. (5), higher maximum shear stress in Eq. (2) which would translate into an additional exit pressure reduction, and thus P_d decrease in Eq. (3). As such, it is likely that this effect increases with increasing inlet pressure and skewing the data toward lower P_d in Fig. 2(f). One evidence of this phenomenon is the increase of normal force with shear rate during the rheological characterization of the EL inks shown in Fig. 3(a). Here, this steady increase coming from the inks confined in between the testing plates can be interpreted as the inks' tendency to expand. Furthermore, the high-magnification image of EL3 exiting the nozzle at high shear rates (Fig. 3(b)) clearly shows the die-swell behavior. Die-swell effect can also be the primary reason behind the decrease (or increase in the absolute value in the negative sense) in P_d with increasing speed.

The height and the width of the lines printed using the EL inks at various speeds are plotted in Figs. 3(c) and 3(d), respectively. At high speeds, fine structures with width and height as low as 50 and 20 μm , respectively, can be produced width EL1, 2, and 3

using low inlet pressures. As mentioned earlier, with EL0 continuous line formation is not possible for inlet pressures less than 68.95 kPa (10 psi) at 180 mm/s. As such, the minimum achievable continuous line width for EL0 is about 70 μm at this speed. This result shows that the DIW process resolution can be increased through the utilization of the drawing regime using inks with appropriate rheological properties to realize this deposition mechanism.

Figure 3(e) shows the cross-sectional images obtained from an EL3 line that was printed by DIW of 1, 2, 5 and 10 total layers. As shown, the electrolytic inks cannot form multilayered 3D structures as the added layers lead to spreading rather than vertical stacking of the deposited material. The elastic and loss moduli of the electrolytic inks are shown in Fig. 3(f). The low elastic modulus of these inks, particularly due to their low solid concentration, can be considered as the main cause for their inability to achieve 3D stacking.

Anodic Inks and Their Printing. The results of the flow ramp testing for the anodic inks are shown in Fig. 4(a). As shown, the addition of the graphite substantially varied the general rheology of the inks, particularly for AN1, 2, and 3. For these inks, the shear stress increases sharply with increasing shear rate below $\sim 50 \text{ s}^{-1}$ and settles into a lower rate of increase at higher shear rates. Accordingly, the shear thinning effect is amplified at higher shear rates, which can be captured quantitatively by fitting power-law models to this data within various shear rate ranges as given in Table 3. This behavior may be explained by the breaking of coagulated graphite particle networks at high shear rates. The viscosity versus shear rate plots for these inks are shown in Fig. 8(f) in the Appendix.

To study the printing behavior of the anodic inks, the same set of tests was performed as detailed earlier. Similar to the electrolytic inks, the anodic inks with HMW PEO (AN1, 2, and 3) formed continuous lines at a lower inlet pressure compared to AN0. At a printing speed of 180 mm/s, continuous lines from AN1, 2, and 3 were formed at 51.71 kPa (7.5 psi) inlet pressure, where AN0 required 86.18 kPa (12.5 psi). For these inks, determination of the P_d value for different experiments relies on using the correct power-law model representing the ink behavior, which in

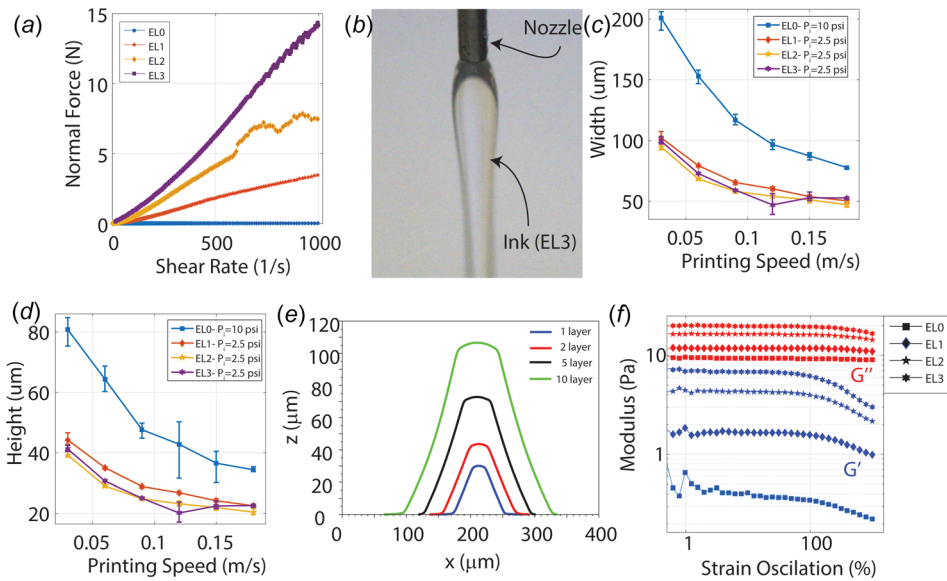


Fig. 3 Results of the DIW experiments with electrolytic inks regarding the printed structure geometry: (a) normal force measured during the flow ramp test of the electrolytic inks indicating the expansion of EL1, 2, and 3 with increasing shear rate, (b) microscopy image of the EL3 ink flowing out of the nozzle indicating the die-swell behavior, (c) width and (d) height of the electrolytic lines as a function of printing speed, (e) cross-sectional profiles of the printed multilayer electrolytic lines, and (f) results of the amplitude sweep of the electrolytic inks

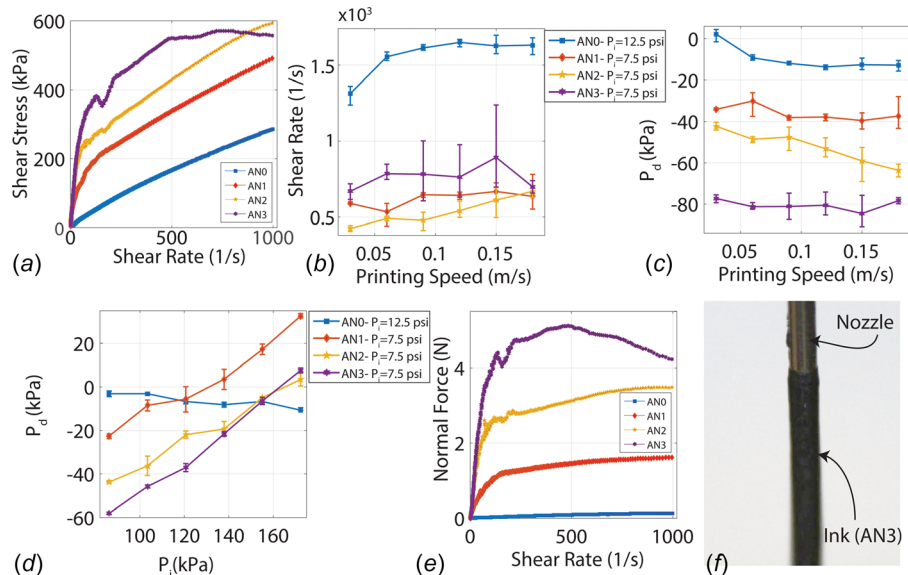


Fig. 4 Results of the rheological characterization and DIW experiments with anodic inks regarding the exit pressure: (a) shear rheology of the anodic inks obtained through the flow ramp test, (b) shear rate of the anodic inks during DIW as a function of printing speed, (c) P_d values calculated for the anodic inks as a function of the printing speed, (d) P_d values calculated for the anodic inks as a function of the inlet pressure, (e) normal force measured during the flow ramp test of the anodic inks, and (f) microscopy image of the AN3 ink flowing out of the nozzle

turn requires knowledge of the shear rates during DIW. As given in Eq. (5), shear rate for the non-Newtonian inks of interest is a function of the flow behavior index (n), thus requires knowledge of the power-law model, yielding an implicit problem. Here, we started with the assumption of the shear rates being higher than 200 s^{-1} and used the associated power-law models for AN1, 2, and 3. We accordingly calculated the shear rates as plotted in Fig. 4(b), showing that the initial assumption was correct. The P_d values calculated using the verified material models and shear

rates are plotted for different inks as a function of printing speeds and inlet pressures are shown in Figs. 4(c) and 4(d), respectively. At an inlet pressure of 51.71 kPa (7.5 psi), high negative values of P_d for AN1, 2, and 3 indicate the prevalence of the drawing regime.

The variation of the P_d value with printing speed and inlet pressure for the anodic inks indicates significant differences in the printing behavior of such inks from the electrolytic ones. Unlike electrolytic inks, the P_d value for these inks showed little variation

Table 3 Power-law coefficients for the anodic inks studied

| Shear rate | 0–50 s ⁻¹ | | 50–200 s ⁻¹ | | >200 s ⁻¹ | |
|------------|----------------------|-------|------------------------|-------|----------------------|-------|
| | K (Pa·s) | n | K (Pa·s) | n | K (Pa·s) | n |
| AN0 | 1.554 | 0.759 | 1.554 | 0.759 | 1.554 | 0.759 |
| AN1 | 14.16 | 0.58 | 28.62 | 0.398 | 16.133 | 0.491 |
| AN2 | 16.85 | 0.677 | 96.74 | 0.213 | 26.448 | 0.451 |
| AN3 | 10.665 | 0.873 | 96.138 | 0.274 | 160.48 | 0.191 |

with the printing speed. Furthermore, at the speed of 60 mm/s, the P_d value for AN1, 2, and 3 increased with increasing inlet pressure, indicating the expected transition from a drawing-dominated deposition to an extrusion-dominated one. These results suggest that the addition of graphite prohibits expansion of the PEO matrix under high shear stresses and rates. A more direct evidence of this conclusion is provided by the normal force measurements recorded during the rheological testing of the anodic inks in Fig. 4(e). As shown, unlike the electrolytic inks, the normal force does not steadily increase with increasing shear rate for the anodic inks. This postulation is further supported by the qualitative observation of the die-swell behavior of the AN3 as it is extruded from the nozzles shown in Fig. 4(f). Compared to the EL3, a substantially less die swell is observed for AN3. This is an expected result that is supported by the earlier findings regarding the die swell of polymer nanocomposites with carbon-based fillers [40].

Height and width variation of the printed anodic lines with respect to various speeds are shown in Figs. 5(a) and 5(b), respectively. The geometry of these lines, printed using the minimum inlet pressure leading to continuous line formation at 180 mm/s, follows a similar behavior as that of the electrolytic lines. One distinct observation that can be made is the variation of the aspect ratio (height/width) of such lines as shown in Fig. 5(c). This ratio is measurably higher for AN1, 2, and 3, which experience the drawing regime, compared to AN0, deposition of which is dominated by extrusion. Furthermore, the aspect ratio shows higher

sensitivity to the printing speed for AN1, 2, and 3: the aspect ratio of the AN0, 1, 2, and 3 lines increased by 2×10^4 , 3×10^4 , 3×10^4 , and 5×10^4 per 1 mm/s printing speed increase, respectively. To further study this effect and the influence on the drawing regime, we printed AN2 at a higher inlet pressure of 72.37 kPa (25 psi), to match the flow rates exhibited by AN0 at 86.18 kPa (12.5 psi) as shown in Fig. 5(d). Under these conditions, the P_d value determined for AN2 is in the positive range, as shown in Fig. 5(e), which can only be observed in the extrusion-only deposition regime, particularly for low nozzle-sample distances [38]. The aspect ratio of the AN2 lines printed at the high inlet pressure shows lower values compared to ones printed at the lower inlet pressure as shown in Fig. 5(f). Compared to the AN0 lines printed at 86.18 kPa (12.5 psi), the AN2 lines printed at 72.37 kPa (25 psi) exhibited lower aspect ratios at lower speeds. However, the aspect ratio increased at a higher rate with increasing printing speed (4×10^4 per 1 mm/s printing speed increase) compared to the AN0 lines. These results suggest that higher aspect ratios are obtained at low flow rates in general. This is an expected result considering the mechanisms governing the evaporation of the ink solvent and the internal flow of the solid inside the ink during this process [41]. Higher absolute mass of the solid deposited leads to further spreading of the ink during the solvent evaporation process leading to a lower aspect ratio. The presence of the drawing regime for inks having HMW PEO enables formation of continuous lines at low flow rates enabling smaller, higher aspect ratio structures. The variation of the aspect ratio with printing speed, on the other hand, seems to be a function of the polymer morphology: the increased HMW PEO content and thus the longer polymer chains in the ink leads to increased aspect ratios at higher printing speeds. One possible explanation for this is the rate-dependent stretching and alignment of the long polymer chains along the printing direction reducing the amount of spreading of the solid content during solvent evaporation.

The results on the multilayer stacking capability of the anodic inks are shown in Fig. 6. To perform this study, lines consisting of different number of layers, 1, 2, 5, and 10 layers, were printed. The cross-sectional profiles of these lines shown in Figs. 6(a) and

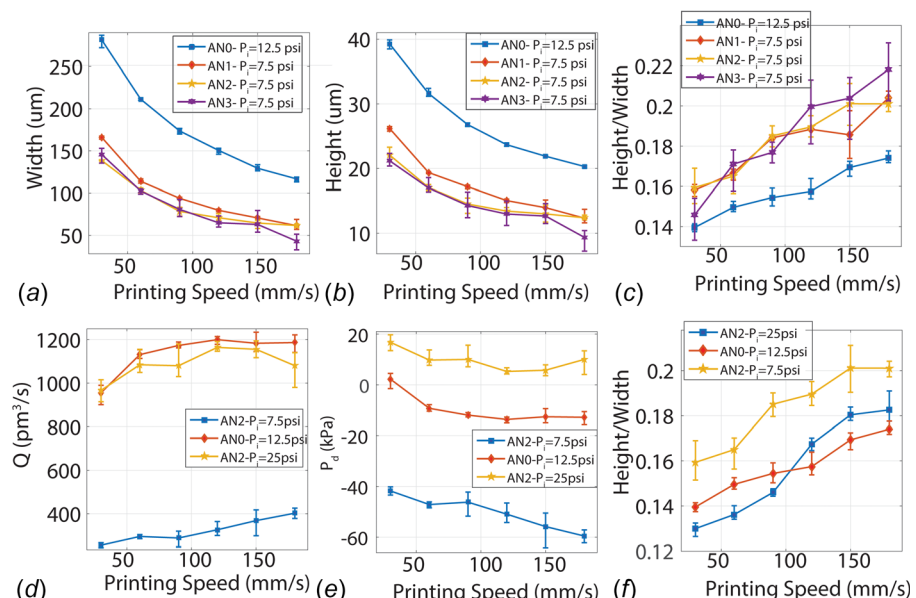


Fig. 5 Results of the DIW experiments with anodic inks regarding the printed structure geometry: (a) width and (b) height of the anodic lines as a function of printing speed, (c) the aspect ratio of the anodic lines as a function of the printing speed, (d) flow rate of the AN0 and AN2 inks under various inlet pressures, (e) P_d values calculated for AN0 and AN2 inks under various inlet pressures, and (f) aspect ratio of the AN0 and AN2 lines printed under various inlet pressures

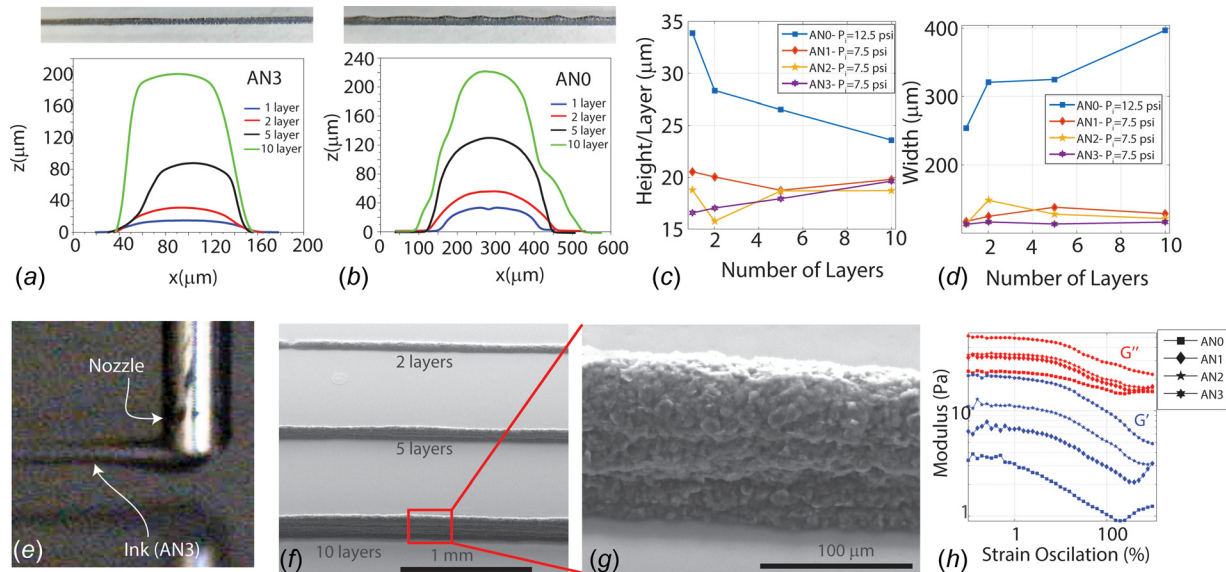


Fig. 6 Results of the DIW experiments with anodic inks regarding multilayer stacking: (a) cross-sectional profiles of the multilayer AN3 lines, top inset: stereo microscopy image of the ten layer AN3 line, (b) cross-sectional profiles of the multilayer AN0 lines, top inset: stereo microscopy image of the ten layer AN0 line, (c) height/number of layers and (d) width of the anodic lines as a function of number of layer printed, (e) the microscopy image of the AN3 as it is printed, (f) and (g) SEM images of the multilayer AN3 lines, and (h) results of the amplitude sweep of the anodic inks

6(b) show substantially better stacking of the layers is achieved with the anodic inks compared to the electrolytic inks.

Furthermore, the anodic inks printed under the effect of the drawing regime exhibited better performance as shown. When the ten layer lines printed with AN3 at 51.71 kPa (7.5 psi) and AN0 at 86.18 kPa (12.5 psi) are compared (top insets in Figs. 6(a) and 6(b), respectively), it can be clearly observed that a more homogeneous structures are obtained under the drawing regime, while significant height and width variations are present under the pure extrusion regime as the layers stack up. To quantify the 3D-stacking performance, the variation of average height/layer and width with the increasing number of layers is shown in Figs 6(c) and 6(d), respectively. For ideal stacking or no spreading, one would expect the height to increase by the same amount at every layer while width stays unchanged. The spreading affects will lead to reduction in the height increase with each layer and increase of the width. The anodic inks undergoing drawing type deposition exhibited close-to-ideal behavior as shown. This result indicates that addition of new layers of material does not lead to redistribution and spreading of the already printed layers, for AN1, 2, and 3 under the tested conditions. Given that the drawing regime is highly prevalent during the deposition of these inks, as shown in Fig. 6(e), one can observe the formation of a filament that trails the nozzle in a near horizontal configuration ($\theta \approx 90$ deg). This filament does not come in contact with the printed layers for a finite amount of time during which solvent evaporation takes place, increasing the solid concentration at the moment it comes in contact with the bottom layer and reducing the amount of spreading.

The SEM images of the multilayer lines printed using AN3 are shown in Figs. 6(f) and 6(g). The side wall morphology of the ten layer line shows some footprints of multilayer stacking. However, substantially better layer-to-layer fusion compared to earlier examples of filamentary DIW [11]. This can be primarily correlated to the lower concentration of these inks compared to the ones used in the literature, leading to the solvent in the added layers partially dissolving the previous layer and enabling better fusion. To analyze the demonstrated multilayer capability of the anodic inks with respect to the ink rheology, we measured their elastic and loss moduli as shown in Fig. 6(h). Compared to the electrolytic inks, both moduli of the anodic inks are higher, as

expected. One critical observation that can be made here is that all the AN inks exhibit lower elastic modulus than the loss modulus, which is considered to be a limiting factor in 3D capabilities of such inks [42]. This study shows that utilization of the drawing regime during DIW can overcome this limitation.

The critical functional property of the anodic inks and the printed structures is their electrical conductivity realized by the added graphite. As such, it is necessary to understand the effect of DIW process on the electrical conductivity of the printed structures. Figure 7(a) shows the variation of electrical resistivity for the AN0 and three lines with respect to the printing speed. As shown, the two materials exhibit similar levels of electrical conductivity when printed at 30 mm/s. However, the conductivity of AN3 is substantially lower than that of AN0 at 90 mm/s and 180 mm/s, with reducing conductivity with printing speed. This result points to the potential effect of the drawing regime on the morphology of the printed structures, particularly the graphite distribution and their percolation networks. Figures 7(d) and 7(f) present the representative AFM topography images obtained from AN3 structures printed at 30 mm/s and 180 mm/s, respectively, showing the graphite flakes embedded inside the PEO matrix. The graphite and matrix phases can be more clearly distinguished through the deformation maps shown in Figs. 7(e) and 7(g), where the rigid graphite phase and the soft PEO matrix can be identified by the low and high deformation (darker regions indicate lower deformation, harder surface), respectively. It can be qualitatively observed from these images that the average size of the detected graphite flakes is smaller for the high-speed structures. Even though it is difficult to reach a detailed conclusion on the graphite morphology through the surface analysis provided by the PFQNM characterization, it is likely that the drawing regime and the associated ink deformation influence the graphite network morphology, leading to less likely contact between the flakes and reduced conductivity. This observation is in accordance with the results reported in the literature on the effect of elongational flow on the filler morphology in polymer nanocomposites [43–45]. Another possible reason for reduced conductivity is the variation of the PEO-LiCO₄ complex microstructure under the drawing regime. Author's earlier work showed that both PEO and LiCO₄ may exhibit crystallinity within the complex at different compositions

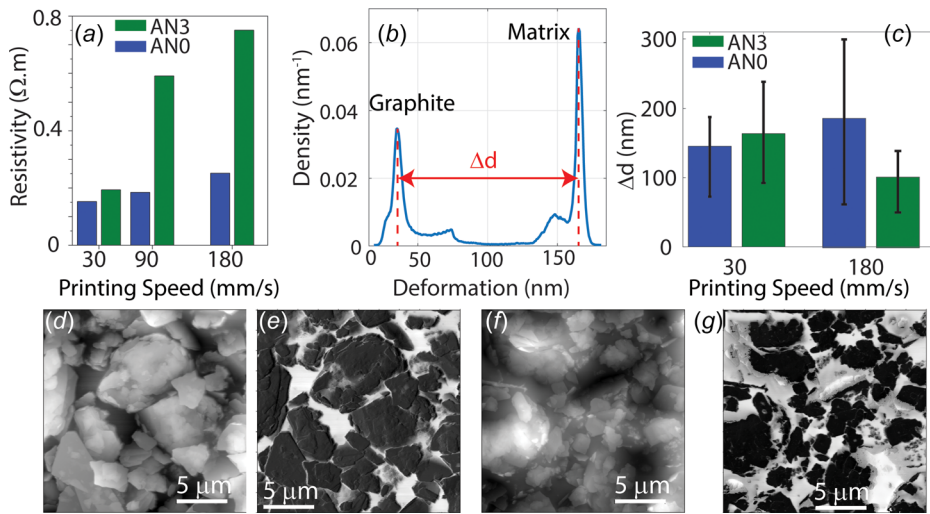


Fig. 7 Electrical conductivity and morphology of the printed anodic structures: (a) variation of the electrical resistivity of AN0 and AN3 lines printed under various speeds, (b) statistical distribution of the deformation data obtained from PFQNM characterization of the printed anodic lines, (c) PEO matrix-graphite deformation difference for AN0 and AN3 at two printing speed levels, (d) topography and (e) deformation maps of the AN3 lines printed at 30 mm/s, and (f) topography and (g) deformation maps of the AN3 lines printed at 180 mm/s

[8]. The elongational stress and the change in solvent evaporation dynamics induced by the drawing regime may lead to a microstructure with less electron transmission capability.

To further understand the variation of the printed structure morphology and properties of graphite and matrix phases, a quantitative analysis of the deformation maps has been performed. A representative statistical distribution of the data obtained from the deformation maps is shown in Fig. 7(b). Here, the higher and lower deformation peaks of this bimodal distribution correspond to the average polymer matrix and graphite deformation, respectively. It should be noted that the absolute value of these averages may show a variation between different images due to the AFM tip radius [36]. As such, a relative analysis considering the difference between these peaks will reveal objective information particularly about the properties of the polymer matrix as indicated by Δd in Fig. 7(b). Figure 7(c) provides the Δd values determined for AN0 and 3 under different printing speeds. In these plots, error bars represent the six different areas scanned from the printed structures. For the low-speed cases, the average Δd values are approximately the same for AN0 and AN3 as shown. AN3 structures differ from the AN0 structures by the decreased average relative deformation of the polymer matrix at high-printing speeds. This result can be interpreted as the hardening of the polymer matrix under the high rate deformation it experiences during the drawing-dominated deposition. This observation is in line with the possibility of microstructure variation of the polymer matrix as noted earlier. These measurements representing a limited total area of the printed structures do not provide an absolute measure of the materials' mechanical properties. However, they indicate measurable effects of the deposition regime on the final properties of the printed line, in accordance with the geometrical and conductivity related observations presented earlier.

Conclusions

In this paper, we presented the DIW of two types of CVPCs consisting of lithium salts and electrically conductive graphite particles inside a PEO polymeric matrix. Particularly, we studied the effect of PEO type, filler type, and DIW parameters on the deposition mechanism that varies between drawing and extrusion.

To this end, we utilized a practical method of modeling the ink flow as viscous non-Newtonian flow through the nozzles and capturing the viscoelastic extensional flow (drawing effects) through the reduction in the nozzle exit pressure. Our study showed that increased amount of high molecular weight PEO leads to increased drawing effects, while increasing dispensing pressure promoted the extrusion mechanism. Under the drawing effects, substantially lower dispensing pressures were required to print continuous lines and the printed structures exhibited higher aspect ratios and better 3D-stacking capability. Furthermore, we demonstrated that the drawing type deposition and high-speed printing lead to lower electrical conductivity and decreased polymer matrix elasticity. As such, this study revealed previously unexplored relationships between the ink composition-DIW parameters and printed structure properties for composite inks. Further studies are required to generalize these findings to (1) a wider range of process parameters including nozzle size, printing distance, etc., (2) different types of CVPCs or polymer composites in general, and (3) more complex geometries.

These findings will inform the DIW ink and process design toward high precision control of the geometry, morphology, and functional properties of 3D-printed CVPCs. On ink design, one critical conclusion is that drawing type deposition can be promoted by addition of minute amounts of HMW polymers to the inks without significantly altering the ink composition. This will help increase the process resolution by enabling printing of finer structures with good 3D-stacking capability, while reducing the input pressure required to achieve continuous deposition at higher speeds. On process design, this study shows that one can switch between extrusion and drawing type deposition by primarily increasing the inlet pressure. This enables utilization of various capabilities of each deposition mechanism in a single printed part, providing opportunities to create hierarchical structures with dimensions ranging from single digit microns to millimeter scales. Finally, the results on the electrical conductivity variation with ink and printing parameters inform CVPC printing applications that special attention has to be paid on during DIW of these materials. Further investigation on the material-process–property relationships will enable control over these properties through the process parameters, realizing the capability to fabricate functionally graded structures.

Considering the wide range of applications that utilize such materials, application of the presented approach and the specific findings will substantially impact a number critical technologies including biological and chemical sensing, printed electronics, electromagnetic interference shielding, and anticorrosion coatings. Particularly, critical impact of this work would be in the area of solid-state energy storage as the inks presented in this study can be used as battery components for Li-ion batteries [8,35]. The high-resolution DIW of these materials to fabricate 3D microelectrode and electrolyte structures carries a great potential for high energy density, flexible batteries that can be integrated with printed electronics [10,11]. Future work will involve (1) developing a more complete process model toward accurately predicting deposition regime, as a function of the ink properties and DIW parameters by incorporating the die-swell effects, (2) performing in-depth studies on the DIW process–morphology–property relationships and underlying mechanisms, and (3) expanding the studies toward more complex geometries such as curvilinear structures and hierarchical parts with multiple size scales.

Acknowledgment

The authors would like to acknowledge Dr. Indranath Dutta and Dr. Hanry Wang of Washington State University for their assistance with the optical interferometry measurements.

Nomenclature

- a = length of the nozzle (m)
- A = cross-sectional area of the printed lines (m^2)
- b = radius of curvature of the pendant drop (m)
- c = volumetric ink concentration (m^3/m^3)
- D = diameter of the nozzle (m)
- D_e = maximum diameter of the pendant drop (m)
- D_s = the diameter of the pendant drop D_e above the bottom of the drop
- f = printing speed (m/s)
- g = gravitational constant (m/s^2)
- H = surface tension correction factor
- K = consistency index ($\text{Pa}\cdot\text{s}^n$)
- L = length of the printed lines (m)
- m_x = mass of ink component x (kg)
- n = flow behavior index
- P_i = relative dispensing pressure (Pa)
- P_{ex} = relative pressure at the exit of the nozzle (Pa)
- P_d = drawing pressure (Pa)
- Q = volumetric ink flow rate (m^3/s)
- R = electrical resistance of the printed lines (Ω)
- r_x = ratio of the mass concentration to density of ink component x (m^3/kg)
- v_x = specific volume of ink component x (m^3/kg)
- V_x = volume of ink component x (m^3)
- w = width of the printed lines (m)
- w = mass concentration of ink solute to inks solvent (kg/kg)
- $z(x,y)$ = height profile of the printed structures as a function of the coordinate along the line length (x) and line width (y) (m)
- $\dot{\gamma}$ = shear rate (s^{-1})
- ρ = electrical resistivity ($\Omega \text{ m}$)
- σ = ink surface tension (Pa m)
- τ = shear stress (Pa)

Appendix

A.1 Determination of the Ink Volumetric Concentration and Density

The electrolytic and the anodic inks studied in this work were prepared with controlled mass compositions. Since they involve solutions of PEO and LiClO₄ in acetonitrile and suspension of

graphite particles in this solution, estimation of the volumetric concentration should take into account the solute–solvent interactions between the PEO, LiClO₄, and the acetonitrile. Cruz et al. showed in their work [37] involving the solution of PEG in water that the specific volume of a solution is given by

$$v = \frac{1+w}{\rho_{\text{solution}}} = v_{\text{solvent}}^0 + v_{\text{solute}}^{-\infty} w + \sum_{n=2}^{\infty} v_n w^n \quad (\text{A1})$$

where $w = (m_{\text{solute}}/m_{\text{solvent}})$, $\rho_{\text{solution}} = (m_{\text{solution}}/V_{\text{solution}}) = (m_{\text{solvent}} + m_{\text{solute}}/V_{\text{solution}})$, $v_{\text{solvent}}^0 = (V_{\text{solvent}}/m_{\text{solvent}})$, $v_{\text{solute}}^{-\infty} = (V_{\text{solute}}/m_{\text{solute}})$, and V_x and m_x are the volume and mass of any given component, respectively. Here, v_n are the empirical constants and are shown to be negligibly small for the studied polymer solutions at room temperature, which is representative of our work. Furthermore, $v_{\text{solute}}^{-\infty}$ is the specific volume of the solute (consisting of PEO, LiClO₄, and graphite in our case) at infinite dilution, which means no interaction between different solute particles. As such, under infinite dilution one can assume that $V_{\text{solute}} = V_{\text{PEO}} + V_{\text{LiClO}_4} + V_{\text{Graphite}}$. Following these assumptions and substituting, one will get:

$$\begin{aligned} \frac{1 + \frac{m_{\text{solute}}}{m_{\text{solvent}}}}{m_{\text{solvent}} + m_{\text{solute}}} &\cong \frac{V_{\text{solvent}}}{m_{\text{solvent}}} + \frac{V_{\text{solute}} m_{\text{solute}}}{m_{\text{solute}} m_{\text{solvent}}} \xrightarrow{\text{yields}} \\ V_{\text{solution}} &\cong V_{\text{solute}} + V_{\text{solvent}} \cong V_{\text{PEO}} + V_{\text{LiClO}_4} + V_{\text{Graphite}} + V_{\text{solvent}} \end{aligned} \quad (\text{A2})$$

Indicating that the additivity of volumes is a good assumption. Since the mass concentration (c) and density (ρ) of each ink component are known, their ratio (r) can be calculated as follows:

$$r_{\text{component}} = \frac{c_{\text{component}}}{\rho_{\text{component}}} = \frac{m_{\text{component}}}{m_{\text{solution}}} \times \frac{V_{\text{component}}}{m_{\text{component}}} = \frac{V_{\text{component}}}{m_{\text{solution}}} \quad (\text{A3})$$

One can show that, using these ratios calculated for each component and volume additivity, the volumetric concentration of the total solute can be determined as

$$\frac{V_{\text{solute}}}{V_{\text{solution}}} = \frac{r_{\text{PEO}} + r_{\text{LiClO}_4} + r_{\text{Graphite}}}{r_{\text{PEO}} + r_{\text{LiClO}_4} + r_{\text{Graphite}} + r_{\text{Solvent}}} \quad (\text{A4})$$

Similarly, the density of the solution (ink) is given by

$$\frac{m_{\text{solution}}}{V_{\text{solution}}} = r_{\text{PEO}} + r_{\text{LiClO}_4} + r_{\text{Graphite}} + r_{\text{Solvent}} \quad (\text{A5})$$

The volumetric solute concentration and the density of each ink calculated accordingly are given in Table 4 in the Appendix.

A.2 Determination of Ink Surface Tension

The surface tension of the inks was measured using the pendant drop method. Here, inks loaded to the DIW system were flown under an inlet pressure leading to dripping at the nozzle exit, video of which was captured using the system's microscope attachment. The still images extracted from these videos were processed as shown in Fig. 8(b) in the Appendix. Using the highlighted dimensions, the surface tension is calculated by

$$\gamma = (\rho_{\text{ink}} - \rho_{\text{air}})gb^2 \frac{1}{H} \quad (\text{A6})$$

where g is the gravitational constant and H is the correction factor which can be empirically determined as a function of D_e/D_s as [46]

Table 4 The volumetric concentration, density, surface tension, and induced exit pressure difference for all the inks studied

| | Volumetric concentration (%) | Density (kg/m ³) | Surface tension (σ) (N/m) | $2\sigma/D$ (kPa-psi) |
|-----|------------------------------|------------------------------|------------------------------------|-----------------------|
| EL0 | 17.61 | 874.86 | 0.0081 | 0.0812–0.0118 |
| EL1 | 17.63 | 874.95 | N/A | N/A |
| EL2 | 17.62 | 875.03 | N/A | N/A |
| EL3 | 17.61 | 875.11 | 0.0085 | 0.118–0.0172 |
| AN0 | 27.03 | 988.88 | 0.0131 | 0.0854–0.0124 |
| AN1 | 27.02 | 988.97 | N/A | N/A |
| AN2 | 27.02 | 989.06 | N/A | N/A |
| AN3 | 27.00 | 989.15 | 0.0019 | 0.0187–0.00271 |

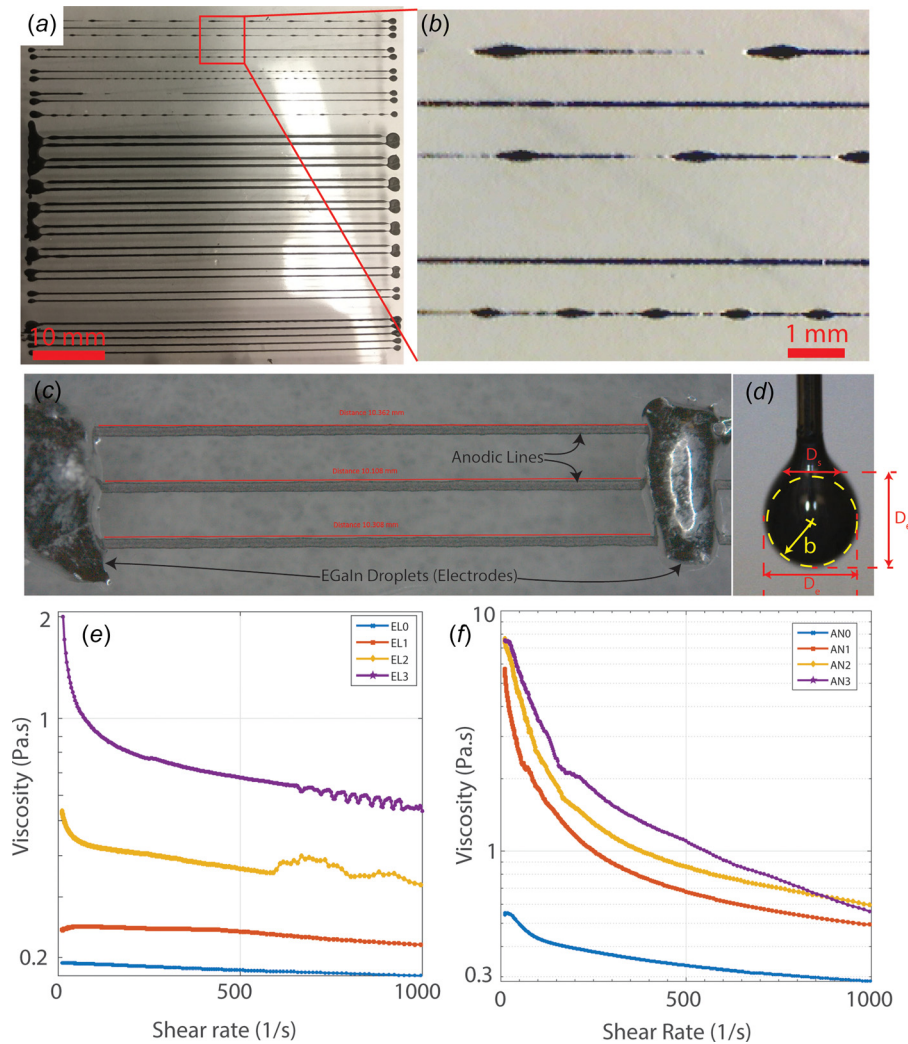


Fig. 8 (a) Optical image showing a set of anodic lines created during the DIW experiments, (b) magnified image of the test lines created to determine the minimum pressure for continuous line printing at 180 mm/s, (c) microscopy image of the electrical measurement configuration for anodic lines highlighting the EGaIn electrodes, (d) microscopy image of an anodic pendant drop used for surface tension measurements, and variation of the viscosity with shear rate for (e) electrolytic inks and (f) anodic inks

$$H = \sqrt{\exp\left(-6.70905 + 15.30025 \frac{D_e}{D_s} - 16.44709 \left(\frac{D_e}{D_s}\right)^2 + 9.92425 \left(\frac{D_e}{D_s}\right)^3 - 2.585035 \left(\frac{D_e}{D_s}\right)^4\right)} \quad (\text{A7})$$

Using the surface tension values calculated for each ink, the exit pressure difference induced due to surface tension is calculated through $2\sigma/D$, where σ is the surface tension and D is the nozzle diameter equal to 200 μm . The surface tension and the induced exit pressure were calculated only for EL0, EL3, AN0, and AN3 as these inks represent the extremes. The calculated values are given in Table 4 in the Appendix.

References

- [1] Muth, J. T., Vogt, D. M., Truby, R. L., Mengüç, Y., Kolesky, D. B., Wood, R. J., and Lewis, J. A., 2014, "Embedded 3D Printing of Strain Sensors Within Highly Stretchable Elastomers," *Adv. Mater.*, **26**(36), pp. 6307–6312.
- [2] Guo, S.-Z., Yang, X., Heuzey, M.-C., and Therriault, D., 2015, "3D Printing of a Multifunctional Nanocomposite Helical Liquid Sensor," *Nanoscale*, **7**(15), pp. 6451–6456.
- [3] Aleman, B., Reguero, V., Mas, B., and Vilatela, J. J., 2015, "Strong Carbon Nanotube Fibers by Drawing Inspiration From Polymer Fiber Spinning," *ACS Nano*, **9**(7), pp. 7392–7398.
- [4] Huang, S., Zhao, C., Pan, W., Cui, Y., and Wu, H., 2015, "Direct Writing of Half-Meter Long CNT Based Fiber for Flexible Electronics," *Nano Lett.*, **15**(3), pp. 1609–1614.
- [5] Potts, J. R., Dreyer, D. R., Bielawski, C. W., and Ruoff, R. S., 2011, "Graphene-Based Polymer Nanocomposites," *Polymer*, **52**(1), pp. 5–25.
- [6] Li, W., Li, F., Li, H., Su, M., Gao, M., Li, Y., Su, D., Zhang, X., and Song, Y., 2016, "Flexible Circuits and Soft Actuators by Printing Assembly of Graphene," *ACS Appl. Mater. Interfaces*, **8**(19), pp. 12369–12376.
- [7] Fassler, A., and Majidi, C., 2015, "Liquid-Phase Metal Inclusions for a Conductive Polymer Composite," *Adv. Mater.*, **27**(11), pp. 1928–1932.
- [8] Wang, Y., Gozen, A., Chen, L., and Zhong, W.-H., 2017, "Gum-Like Nanocomposites as Conformable, Conductive, and Adhesive Electrode Matrix for Energy Storage Devices," *Adv. Energy Mater.*, **7**(6), p. 1601767.
- [9] Wang, Y., Li, B., Ji, J., Eyler, A., and Zhong, W.-H., 2013, "A Gum-Like Electrolyte: Safety of a Solid, Performance of a Liquid," *Adv. Energy Mater.*, **3**(12), pp. 1557–1562.
- [10] Hu, J., Jiang, Y., Cui, S., Duan, Y., Liu, T., Guo, H., Lin, L., Lin, Y., Zheng, J., Amine, K., and Pan, F., 2016, "3D-Printed Cathodes of $\text{LiMn}_{1-x}\text{Fe}_x\text{PO}_4$ Nanocrystals Achieve Both Ultrahigh Rate and High Capacity for Advanced Lithium-Ion Battery," *Adv. Energy Mater.*, **6**(18), p. 1600856.
- [11] Sun, K., Wei, T.-S., Ahn, B. Y., Seo, J. Y., Dillon, S. J., and Lewis, J. A., 2013, "3D Printing of Interdigitated Li-Ion Microbattery Architectures," *Adv. Mater.*, **25**(33), pp. 4539–4543.
- [12] Decker, B. Y., and Gan, Y. X., 2015, "Electric Field-Assisted Additive Manufacturing Polyaniline Based Composites for Thermoelectric Energy Conversion," *ASME J. Manuf. Sci. Eng.*, **137**(2), p. 024504.
- [13] Majesté, J.-C., 2012, "Rheology and Processing of Polymer Nanocomposites: Theory, Practice, and New Challenges," *Rheology and Processing of Polymer Nanocomposites*, S. Thomas, R. Muller, and J. Abraham, eds., Wiley, Hoboken, NJ, pp. 69–134.
- [14] Lewis, J., and Gratson, G., 2004, "Direct Writing in Three Dimensions," *Mater. Today*, **7**(7–8), pp. 32–39.
- [15] Hon, K. K. B., Li, L., and Hutchings, I. M., 2008, "Direct Writing Technology—Advances and Developments," *CIRP Ann. Manuf. Technol.*, **57**(2), pp. 601–620.
- [16] Lewis, J. A., 2006, "Direct Ink Writing of 3D Functional Materials," *Adv. Funct. Mater.*, **16**(17), pp. 2193–2204.
- [17] Truby, R. L., and Lewis, J. A., 2016, "Printing Soft Matter in Three Dimensions," *Nature*, **540**(7633), pp. 371–378.
- [18] Berry, S. M., Pabba, S., Cohn, R. W., and Keynton, R. S., 2012, "Direct-Write Drawing of Carbon Nanotube/Polymer Composite Microfibers," *J. Nanomater.*, **2012**, p. 690301.
- [19] Berry, S. M., Harfenist, S. A., Cohn, R. W., and Keynton, R. S., 2006, "Characterization of Micromanipulator-Controlled Dry Spinning of Micro- and Sub-Microscale Polymer Fibers," *J. Micromech. Microeng.*, **16**(9), pp. 1825–1832.
- [20] Harfenist, S. A., Cambron, S. D., Nelson, E. W., Berry, S. M., Isham, A. W., Crain, M. M., Walsh, K. M., Keynton, R. S., and Cohn, R. W., 2004, "Direct Drawing of Suspended Filamentary Micro- and Nanostructures From Liquid Polymers," *Nano Lett.*, **4**(10), pp. 1931–1937.
- [21] Berry, S. M., Pabba, S., Crest, J., Cambron, S. D., McKinley, G. H., Cohn, R. W., and Keynton, R. S., 2011, "Characterization and Modeling of Direct-Write Fabrication of Microscale Polymer Fibers," *Polymer*, **52**(7), pp. 1654–1661.
- [22] Zheng, G., Yu, Z., Zhuang, M., Wei, W., Zhao, Y., Zheng, J., and Sun, D., 2014, "Electrohydrodynamic Direct-Writing of Three-Dimensional Multi-Loop Nanofibrous Coils," *Appl. Phys. A Mater. Sci. Process.*, **116**(1), pp. 171–177.
- [23] Zheng, G., Sun, L., Wang, X., Wei, J., Xu, L., Liu, Y., Zheng, J., and Liu, J., 2016, "Electrohydrodynamic Direct-Writing Microfiber Patterns Under Stretching," *Appl. Phys. A*, **122**(2), p. 112.
- [24] Cai, Y., Li, J., Poh, C. K., Tan, H. C., San Thian, E., Hsi Fuh, J. Y., Sun, J., Tay, B. Y., and Wang, W., 2013, "Collagen Grafted 3D Polycaprolactone Scaffolds for Enhanced Cartilage Regeneration," *J. Mater. Chem. B*, **1**(43), pp. 5971–5976.
- [25] Li, X., Li, Z., Wang, L., Ma, G., Meng, F., Pritchard, R. H., Gill, E. L., Liu, Y., and Huang, Y. Y. S., 2016, "Low-Voltage Continuous Electrospinning Patterning," *ACS Appl. Mater. Interfaces*, **8**(47), pp. 32120–32131.
- [26] Collino, R. R., Ray, T. R., Fleming, R. C., Cornell, J. D., Compton, B. G., and Begley, M. R., 2016, "Deposition of Ordered Two-Phase Materials Using Microfluidic Print Nozzles With Acoustic Focusing," *Extreme Mech. Lett.*, **8**, pp. 96–106.
- [27] Barnes, H. A., and Walters, K., 1989, *An Introduction to Rheology*, Elsevier, Amsterdam, The Netherlands.
- [28] Chhabra, R. P., and Richardson, J. F., 1999, *Non-Newtonian Flow: Fundamentals and Engineering Applications*, Butterworth-Heinemann, Woburn, MA.
- [29] Bruneaux, J., Therriault, D., and Heuzey, M.-C., 2008, "Micro-Extrusion of Organic Inks for Direct-Write Assembly," *J. Micromech. Microeng.*, **18**(11), p. 115020.
- [30] Chen, X. B., and Ke, H., 2006, "Effects of Fluid Properties on Dispensing Processes for Electronics Packaging," *IEEE Trans. Electron. Packag. Manuf.*, **29**(2), pp. 75–82.
- [31] Chen, X. B., Li, M. G., and Ke, H., 2008, "Modeling of the Flow Rate in the Dispensing-Based Process for Fabricating Tissue Scaffolds," *ASME J. Manuf. Sci. Eng.*, **130**(2), p. 021003.
- [32] Chung, J. H. Y., Naficy, S., Yue, Z., Kapsa, R., Quigley, A., Moulton, S. E., and Wallace, G. G., 2013, "Bio-Ink Properties and Printability for Extrusion Printing Living Cells," *Biomater. Sci.*, **1**(7), pp. 763–773.
- [33] Noman Hasan, M., Vatani, M., Chandy, A., and Choi, J.-W., 2016, "Experimental and Numerical Analysis of Filament Front Deformation for Direct-Print," *ASME J. Manuf. Sci. Eng.*, **138**(1), p. 011003.
- [34] Xue, Z., He, D., and Xie, X., 2015, "Poly(Ethylene Oxide)-Based Electrolytes for Lithium-Ion Batteries," *J. Mater. Chem. A*, **3**(38), pp. 19218–19253.
- [35] Wang, Y., Zhong, W.-H., Schiff, T., Eyler, A., and Li, B., 2015, "A Particle-Controlled, High-Performance, Gum-Like Electrolyte for Safe and Flexible Energy Storage Devices," *Adv. Energy Mater.*, **5**(2), p. 1400463.
- [36] Pittenger, B., Erina, N., and Su, C., 2009, "Quantitative Mechanical Property Mapping at the Nanoscale With PeakForce QNM," Bruker Instruments, Beijing, China, Report No. 128.
- [37] Cruz, R. D. C., Martins, R. J., Cardoso, M. J. E. D. M., and Barcia, O. E., 2009, "Volumetric Study of Aqueous Solutions of Polyethylene Glycol as a Function of the Polymer Molar Mass in the Temperature Range 283.15 to 313.15 K and 0.1 MPa," *J. Solution Chem.*, **38**(8), pp. 957–981.
- [38] Li, B., Clark, P. A., and Church, K. H., 2007, "Robust Direct-Write Dispensing Tool and Solutions for Micro/Meso-Scale Manufacturing and Packaging," *ASME Paper No. MSEC2007-31037*.
- [39] Clasen, C., Phillips, P. M., Palangetic, L., and Vermant, J., 2012, "Dispensing of Rheologically Complex Fluids: The Map of Misery," *AIChE J.*, **58**(10), pp. 3242–3255.
- [40] Dangtunjee, R., and Supaphol, P., 2008, "Melt Rheology and Extrudate Swell of Titanium (IV) Oxide Nanoparticle-Filled Isotactic Polypropylene: Effects of Content and Surface Characteristics," *Polym. Test.*, **27**(8), pp. 951–956.
- [41] Semenov, S., Trybala, A., Rubio, R. G., Kovalchuk, N., Starov, V., and Velarde, M. G., 2014, "Simultaneous Spreading and Evaporation: Recent Developments," *Adv. Colloid Interface Sci.*, **206**, pp. 382–398.
- [42] Osterbur, L., 2013, "3D Printing of Hyaluronic Acid Scaffolds for Tissue Engineering Applications," *M.S. thesis*, University of Illinois at Urbana-Champaign, Champaign, IL.
- [43] Compton, B. G., and Lewis, J. A., 2014, "3D-Printing of Lightweight Cellular Composites," *Adv. Mater.*, **26**(34), pp. 5930–5935.
- [44] Park, J. H., and Joo, Y. L., 2014, "Tailoring Nanorod Alignment in a Polymer Matrix by Elongational Flow Under Confinement: Simulation, Experiments, and Surface Enhanced Raman Scattering Application," *Soft Matter*, **10**(19), pp. 3494–3505.
- [45] Okamoto, M., Nam, P., Maiti, P., Kptaka, T., Hasegawa, N., and Usuki, A., 2001, "A House of Cards Structure in Polypropylene/Clay Nanocomposites Under Elongational Flow," *Nano Lett.*, **1**(6), pp. 295–298.
- [46] Arashiro, E. Y., and Demarquette, N. R., 1999, "Use of the Pendant Drop Method to Measure Interfacial Tension Between Molten Polymers," *Mater. Res.*, **2**(1), pp. 23–32.